Consistent Seagrass Mapping Across Various Tide Levels From Planet SuperDove Images

Siyuan Hou, Xiaolong Yu, Wendian Lai, Fei Zhang, Hanyang Qiao, Peng Cheng, and Zhongping Lee, *Member, IEEE*

***Abstract*— Seagrass meadows are vital blue carbon ecosystems, and remote sensing provides a cost-effective means of monitoring their changes at high spatiotemporal resolution. While existing algorithms excel in low-tide mapping, accurately and consistently identifying seagrass at mid-to-high tide levels remains challenging. This study presents a support vector machine (SVM)-based substrate classification model (SCM_SVM) for automated seagrass identification across various tidal conditions using Planet SuperDove imagery, with a demonstration provided for the Li'An Lagoon (LAL). By training with ∼1.8 million matched ground-truth substrate data and Rayleigh scattering-corrected top-of-atmosphere reflectance (ρ_{rc}), SCM_SVM could robustly identify seagrass from SuperDove ρ_{rc} measurements across low-to-high tide levels. Validation against independent field measurements indicated a detection accuracy of seagrass exceeding 85%. Notably, SCM_SVM provided consistent seagrass distributions in spatial patterns and extents for images acquired under different tidal levels. Time-series analysis from 2021 to 2023 revealed a significant decline of −0.15 km^2/yr in the area. These results underscore the potential of SuperDove for high spatiotemporal resolution monitoring of seagrass dynamics. Future work will focus on enhancing the global applicability of SCM_SVM and extending it to detect other submerged vegetation.**

***Index Terms*— High tide, remote sensing, seagrass mapping, SuperDove.**

I. Introduction

SEAGRASSES, underwater angiosperms thriving in tropical and temperate regions, constitute a pivotal component of shallow coastal marine ecosystems [1], [2], [3]. Seagrasses provide essential habitats and nourishment for various marine organisms, mitigating the impacts of currents and waves while regulating sediment deposition and erosion [4], [5]. Furthermore, seagrass beds are recognized as significant contributors to marine blue carbon through photosynthesis [6], [7], [8], providing 10%–15% of the ocean's total carbon and 50% of particulate organic carbon sequestration despite covering only 0.2% of the ocean's surface area [9], [10], [11]. However, seagrass growth is highly vulnerable to human activities, extreme events, and climate change [12], [13]. Globally, seagrass coverage declines rapidly at approximately 7% per year, with an escalating degradation trend [3], [14]. Therefore, timely and large-scale monitoring approaches are crucial for the conservation and management of seagrass ecosystems [15], [16].

Monitoring seagrass distributions involves two primary approaches, i.e., field investigations and remote sensing techniques [17], [18]. Field investigations encompass in situ sampling, underwater photography, and sonar detection [19], [20], providing the baseline data on seagrass distribution. However, these methods are labor-intensive and have limited spatial and temporal coverage, making it challenging to understand large-scale seagrass dynamics comprehensively [21]. Satellite remote sensing, characterized by extensive spatial coverage and frequent revisits, has emerged as an essential approach in seagrass monitoring, with many seagrass detection algorithms developed in recent years [22]. These algorithms primarily rely on the empirical or semi-analytical relationships between substrate data and airborne or satellite-borne radiometric measurements. They can be broadly classified into three main categories: spectral index algorithms, semi-analytical algorithms, and machine learning approaches [20], [23].

Spectral index methods differentiate seagrass from other substrates by analyzing the spectral signature of radiometric measurements, such as the remote sensing reflectance [$R_{rs}(\lambda)$], and applying different thresholds of spectral indexes for substrate classification [22], [24]. Semi-analytical algorithms estimate the contribution of the water column and substrate to the measured $R_{rs}(\lambda)$ through radiative transfer models, which can simultaneously predict the substrate type [25], [26], [27], [28]. Machine learning models, including supervised and unsupervised classification techniques, have demonstrated effectiveness in substrate detection and classification [29]. Once trained, algorithms such as random forests, support vector machines (SVMs), and decision trees can automatically classify various substrate types [26], [30], [31], [32]. In addition, target detection-based deep learning models, including DLNN, convolutional neural networks, and UNet, have also been used for seagrass identification [33], [34], [35], [36]. However, the performance of these existing models is highly dependent on the tidal conditions, with most of them only applicable to low-tide scenarios, especially for index-based algorithms [37], [38].

Received 1 November 2024; revised 26 March 2025; accepted 23 May 2025. Date of publication 29 May 2025; date of current version 16 June 2025. This work was supported in part by the National Key Research and Development Program of China under Grant 2022YFC3105402 and in part by the Blue Carbon Ecosystem Assessment, Restoration and Accounting Project (BLUE-CARE) through Tencent. *(Corresponding author: Xiaolong Yu.)*

Siyuan Hou, Wendian Lai, Fei Zhang, Hanyang Qiao, Peng Cheng, and Zhongping Lee are with the State Key Laboratory of Marine Environmental Science, College of Ocean and Earth Sciences, Xiamen University, Xiamen 361102, China (e-mail: siyuanhou@stu.xmu.edu.cn; wendian_lai@163.com; 22320230156507@stu.xmu.edu.cn; 22320210156153@stu.xmu.edu.cn; pcheng@xmu.edu.cn; zhongping.lee@umb.edu).

Xiaolong Yu is with the State Key Laboratory of Marine Environmental Science, College of Ocean and Earth Sciences, and Fujian Provincial Key Laboratory for Coastal Ecology and Environmental Studies, Xiamen University, Xiamen 361102, China (e-mail: xlyu@xmu.edu.cn).

Digital Object Identifier 10.1109/TGRS.2025.3574821

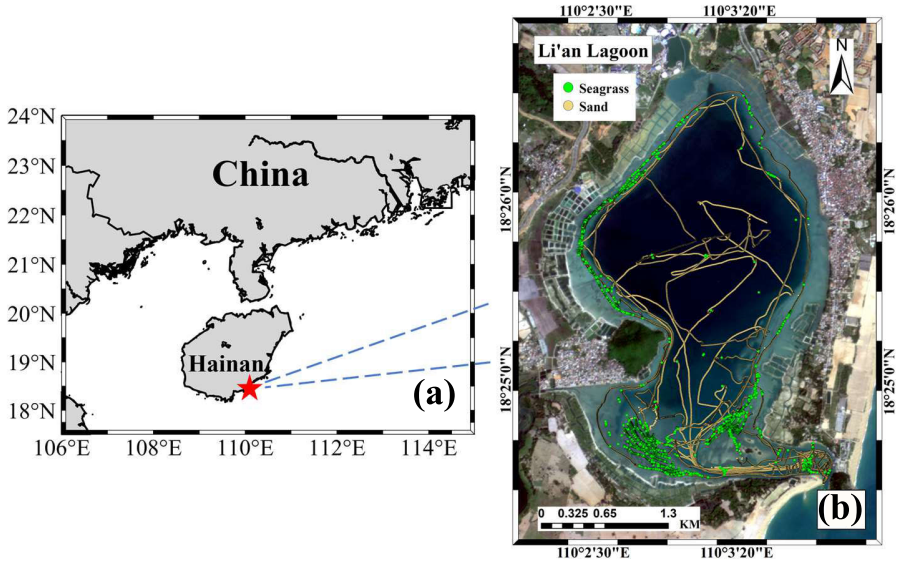

Fig. 1. (a) Location of the LAL in China. (b) True-color composited image of SuperDove acquired on November 5, 2022. The green and yellow dots represent the ground-truth substrates acquired from several field surveys conducted between November 15, 2022 and November 20, 2022, respectively.

Seagrass detection becomes more difficult under high-tide conditions due to the attenuation of bottom reflectance with increasing water depth. At greater depths, the contribution of benthic seagrass to the water-leaving signal may be significantly reduced, making it challenging to distinguish seagrass from other substrates from remote sensing. Additionally, the strong absorption of water in the red and near-infrared (NIR) bands can diminish the effectiveness of index-based algorithms, which typically rely on the relative difference between surface reflectance (SR) at the red and NIR bands [38], [39]. As a result, seagrass meadows are often misidentified or underestimated in distribution maps derived from mid-tide to high-tide images [18], [40]. For machine learning-based models, low-tide imagery is commonly used to enhance the classification accuracy, while the absence of high-tide data restricts both dataset size and model performance under high-tide conditions. Thus, constructing a representative, large-scale training dataset is crucial for accurately detecting seagrass distribution from satellite imagery across varying tidal scenarios. However, research on this aspect remains limited, with relatively few studies incorporating high-tide data into model training and validation.

Another key limitation of seagrass detection through remote sensing is the spatiotemporal resolution of satellite imagery. On the one hand, most seagrass meadows are distributed in narrow and fragmented nearshore areas, making their detection challenging for operational medium-resolution satellites [23]. On the other hand, the revisit time of high-resolution satellites and cloud cover directly affects the number of usable images for the timely assessment of seagrass dynamics [41], [42]. Therefore, satellite imagery with high resolution and revisit frequency would be preferred for seagrass detection in nearshore areas.

This study aims to develop a model that ensures accurate and consistent seagrass mapping across varying tidal scenarios using Planet SuperDove, a SmallSat constellation characterized by high spatiotemporal resolution (3 m, subdaily). To achieve this, we first constructed a training dataset with ~2.3 million matched "ground-truth" substrate data and radiometric measurements from SuperDove images acquired across low to high tide levels in the Li'An Lagoon (LAL). We then developed a machine learning-based model for seagrass detection, validated it against field survey measurements, and applied it to characterize the spatiotemporal variability of seagrass distribution in LAL. Sections II–IV describe the data, methods, results, the model's performance, and limitations.

II. Data and Methods

A. Study Area and Field Surveys

The LAL, situated in Lingshui County, Hainan Province, is centered at 18.42°N and 110.06°E (Fig. 1). This semi-enclosed lagoon covers an area of ~9 km^2, with a maximum depth of 7.6 m and an average depth of 5.1 m. Tides are the primary hydrodynamic forces, with average tide levels ranging from 0.3 to 1.6 m. Seagrass meadows are widely distributed throughout the lagoon, dominated by *Thalassia hemprichii* and *E. acoroides*, which persist throughout the year. Other commonly found species include *Halophila ovalis*, *Zostera marina*, and *Cymodocea rotunda*.

B. Field Survey and Processing

Field surveys were conducted in the LAL from November 15, 2022 to November 20, 2022, to collect ground-truth substrate data using a single-beam echo sounder (SBE, BioSonics DT-X). Specifically, the SBE was mounted on the boat's hull, with the sonar transducer positioned vertically downward to capture signals from the seabed, enabling continuous underway measurements of sonar reflections. All raw data were processed and analyzed using BioSonics Visual Habitat software to estimate seagrass canopy height and water depth [19].

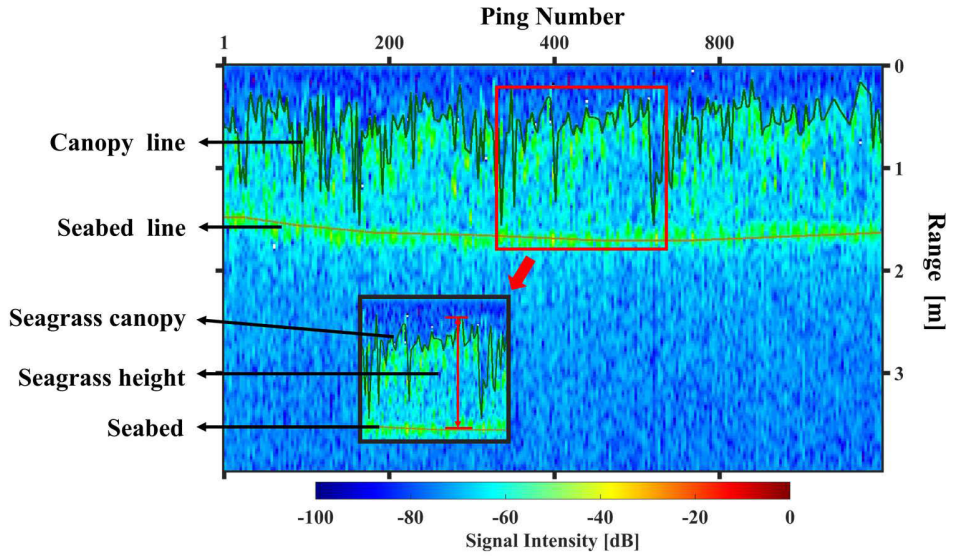

Fig. 2. Example echogram generated by the DT-X echosounder for sonar signal recorded during the field survey. The red line with arrows in the inset figure represents the canopy height.

As an example, the echogram in Fig. 2 highlights the distinct variations in signal intensity when the sonar pulse interacts with different media, including water, seagrass, and seabed. Each medium produces a unique echo response, with signal amplitude varying based on its physical properties. The presence of seagrass or seabed significantly increases signal intensity due to their dense structure, which reflects sound waves more strongly than the surrounding water column. Thus, a canopy or seabed line can be calculated based on the signal density, which is automatically extracted by BioSonics Visual Habitat software. The vertical distance between the seabed and seagrass canopy lines is then calculated to determine the seagrass canopy height.

E. acoroides has an average canopy height of approximately 0.4 m, ranging from 0.1 to 0.8 m [43], whereas *T. hemprichii* averages 0.17 m in canopy height [43]. Thus, we used a canopy height greater than 0.1 m to differentiate seagrass from a sand substrate. Such a threshold could maximize sample inclusion and ensure that smaller seagrass patches are retained in the ground-truth data, enhancing the representativeness of the training data.

The ground-truth data for the distribution of seagrass and sand substrates in LAL were then obtained from the sonar data. Approximately 130 000 ground-truth substrate records were collected, with their spatial distributions presented in Fig. 1(b). The ground-truth seagrass distributions derived from sonar measurements were used solely for the independent validation of support vector machine (SVM)-based substrate classification model (SCM_SVM).

C. Satellite Data and Preprocessing

The Planet constellation, consisting of hundreds of Dove satellites, is the world's largest fleet of SmallSats. Planet launched its first four-band (blue, green, red, and NIR) Dove-Classic (PlanetScope-0) prototype satellite in 2013. Since April 2019, the third-generation SuperDove satellites (PlanetScope-2) have been continuously deployed, featuring enhanced image quality and improved spectral resolution. SuperDove satellites are equipped with eight spectral bands in the visible-to-NIR domain, centered at 444, 492, 533, 566, 612, 665, 707, and 866 nm. With over 200 satellites in orbit, SuperDove provides high-resolution (3 m) and high-frequency (subdaily) imagery for advanced Earth observations. Although PlanetScope has been widely used for the remote sensing interpretation of seagrass meadows, most of these studies have focused on low-tide and pixel-based imagery analysis [44], [45], without fully addressing the challenges of seagrass detection under high-tide conditions. However, the enhanced spectral information of SuperDove should have the potential to enable more accurate identification of seagrass under different tidal conditions.

Due to the absence of an onboard calibration system, SuperDove achieves a relative calibration through synchronized observations with the Sentinel-2 satellite for top-of-atmosphere reflectance [$\rho(\lambda)$] [46]. Planet's Level-2 SR product, obtained through atmospheric correction using the 6S radiative transfer model, performs well in clear water bodies but is less suitable for nearshore shallow areas [47]. Due to nearshore adjacency effects and challenges in aerosol scattering corrections, atmospheric correction algorithms in nearshore waters often perform poorly, leading to low-quality $R_{rs}(\lambda)$ and occasionally even negative values [48]. In contrast, Rayleigh scattering-corrected reflectance [$\rho_{rc}(\lambda)$] retains aerosol contributions and is less affected by environmental disturbances, significantly enhancing data availability for remote sensing applications in nearshore waters [49], [50].

In this study, we acquired 157 cloud-free SuperDove images of LAL from 2021 to 2023, encompassing all seasons and a range of tidal conditions. All the Level 1 products were processed using Acolite to generate the $\rho_{rc}(\lambda)$ products. The tidal information for each SuperDove acquisition was obtained from a tidal station in the nearby Xincun Lagoon (~30 km from LAL), with tide records sourced from the Global Tide Forecast Service Platform (http://global-tide.nmdis.org.cn).

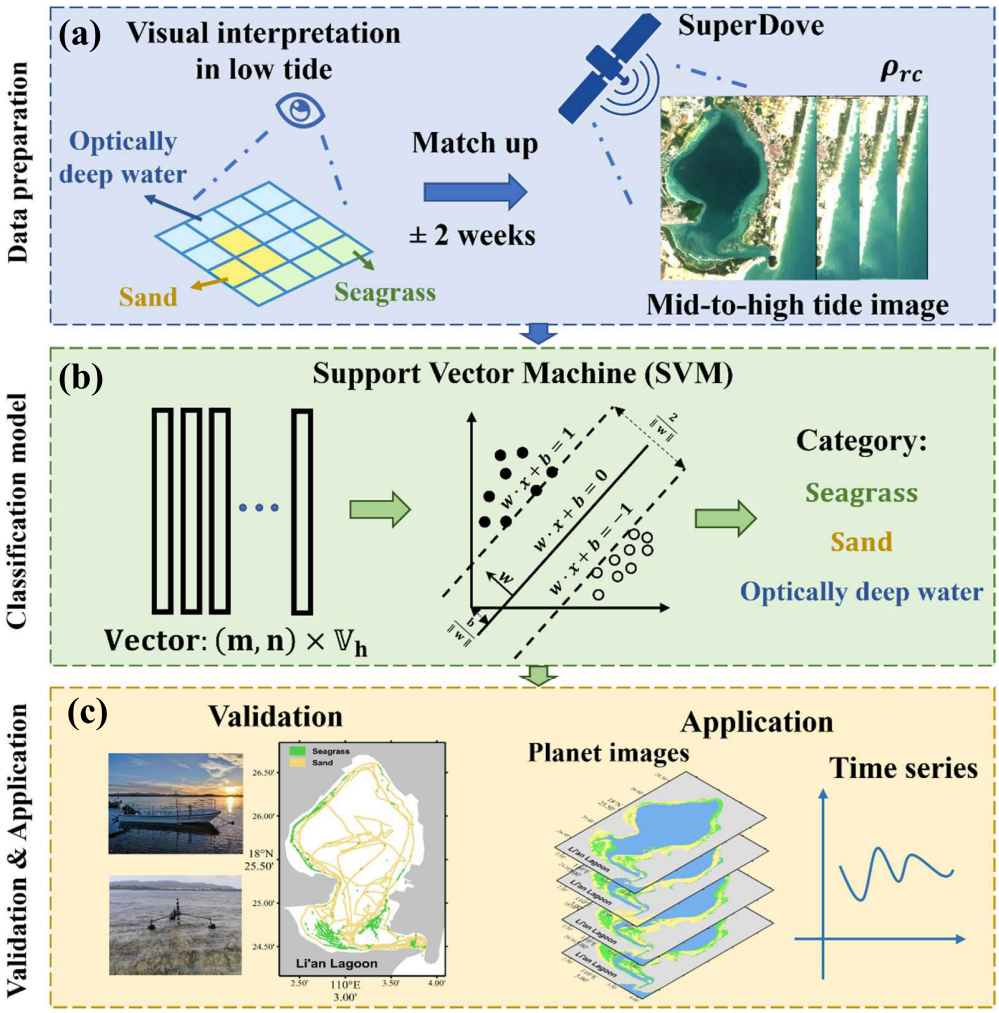

Fig. 3. Proposed framework for seagrass mapping in this study. (a) Construction of the training dataset using matchups between satellite radiometric measurements and groundtruth substrate data. (b) Model development based on machine learning. (c) Model validation and application.

D. Development of the Substrate Classification Model

As illustrated in Fig. 3, the seagrass mapping framework comprises three key modules: the construction of matchups between satellite radiometric measurements and ground-truth substrate data for model training, model development based on machine learning, and model validation and application.

Given the limited spatiotemporal coverage of field-based substrate data, we implemented an alternative approach to obtain ground-truth substrate data. This method leverages the differences in texture, color, and distribution patterns between seagrass and sand substrates during low tide, as illustrated in Fig. 4. Seagrass typically appears as dark gray, irregular patches with distinct textures. In contrast, sand substrates have a lighter color and a more uniform distribution, while optically deep water (ODW) generally appears dark blue. To ensure comprehensive coverage, we collected all available low-tide SuperDove images from 2022 to 2023, encompassing all four seasons, and obtained the "ground-truth" substrate data through visual interpretation. Here, the ground-truth substrate types were categorized into seagrass and sand only. We introduced an additional category, i.e., ODW, to minimize possible misclassification of substrates in ODW where the substrate contributes almost nil to the satellite-observed signal [50]. For simplicity, ODW is also referred to as one of the substrate types in the following.

It is important to note that only pixels located at the center of each substrate patch were selected as ground-truth data, as shown in Fig. 4(a) and (d), as these pixels could have a lower possibility of misclassification. In other words, we selected only pixels with high confidence for each ground-truth substrate type. In addition, the normalized difference vegetation index (NDVI) was also employed as a supplement to constrain the ground-truth seagrass substrate when the tide is extremely low. We did not further distinguish the seagrass species in this effort, as the multispectral $\rho_{rc}(\lambda)$ of the two dominant seagrass species in the LAL exhibited quite similar spectral characteristics, especially for mid- to high-tide scenarios. Finally, we extracted the ground-truth substrate types and their geolocation information using ArcGIS. It is worth pointing out that the distribution of these selected ground-truth substrates in Fig. 4(e) aligns well with our observations from field surveys. Subsequently, the interpreted ground-truth substrates from each low-tide image were used as a reference to match all available $\rho_{rc}(\lambda)$ measurements from SuperDove within two weeks of that image's capture date. In this way, we obtained ~2.3 million

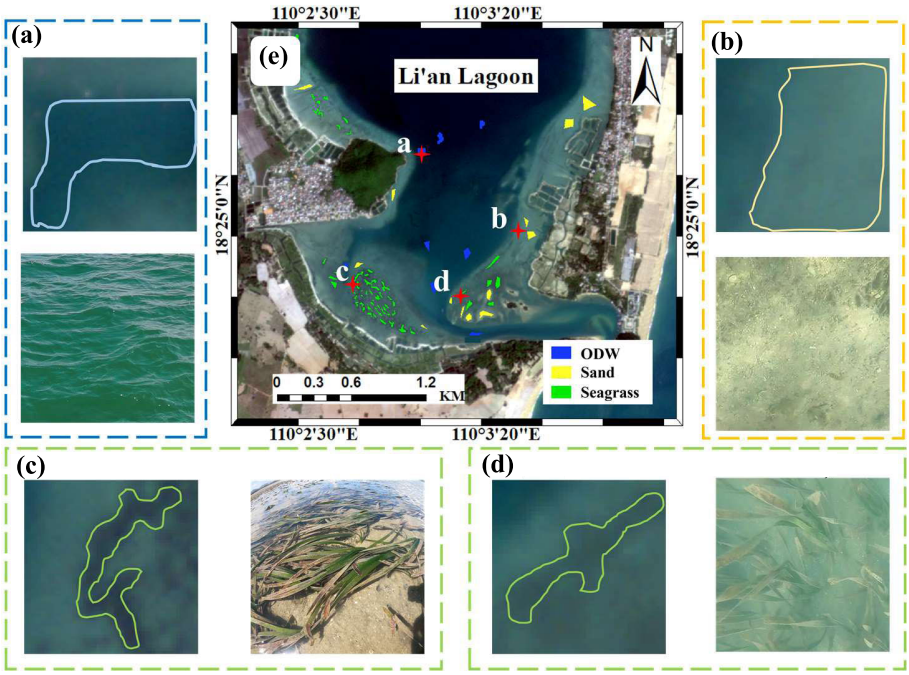

Fig. 4. Demonstration of substrate classification from low-tide images using visual interpretation. (a)–(d) Substrate classification examples for ODW, sand, *Z. marina*, and *E. acoroides*, respectively, with their locations highlighted as red marks in (e). The blue, yellow, and green patches in (e) represent the final extracted ground-truth substrates for ODW, sand, and seagrass, respectively.

matchups between ground-truth substrate types and $\rho_{rc}(\lambda)$ measurements acquired under various tide conditions from low to relatively high tides. This compiled dataset was then used to develop the substrate classification model, where 90% of the data were randomly selected for model training (termed Train_set) and the remaining 10% employed for model testing (termed Test_set). Since this study aims to accurately map seagrass distributions, the training dataset is predominantly composed of seagrass substrates (∼54%), with sand (∼28%) and ODW (∼18%) making up the remainder.

In this study, a machine learning model based on the support vector machine (SVM) was developed for substrate classification, which is hereafter termed SCM_SVM. The input for SCM_SVM consists of $\rho_{rc}(\lambda)$ at the eight SuperDove bands, and the model output classifies substrates into seagrass, sand, and ODW. The SVM model supports linear, polynomial, and radial basis function (RBF) kernels, making it adaptable to various linear or nonlinear data types [51]. The design of SVM is relatively simple, with fewer tunable hyperparameters than other machine learning models. Its performance can be enhanced with longer training times when processing large datasets. The SVM model utilizes hyperplanes to determine the optimal separation space between classes, thereby maximizing the margin between data points and the hyperplane. One of the key advantages of SVM is its accuracy and robustness to outliers [33], [51], [52], making it one of the most widely used machine learning models for substrate classifications [53], [54].

E. Model Intercomparison and Evaluation Metrics

In addition to SCM_SVM, we employed the water-adjusted vegetation index (WAVI) [55] and the submerged seagrass identification index (SSII) [56] for model intercomparison. Specifically, WAVI incorporates an adjustment factor L to correct for water influence, enhancing its effectiveness in aquatic vegetation detection, and is expressed as

$$\text{WAVI} = (1+L)\frac{\rho_{rc}(865)-\rho_{rc}(490)}{\rho_{rc}(865)+\rho_{rc}(490)+L} \tag{1}$$

where L ranges from 0 to 1 and is set to 0.5 in this study, a typical value that effectively reduces background interference for medium vegetation cover [22]. Higher WAVI values indicate stronger responses from medium- to high-density aquatic vegetation.

SSII, on the other hand, is specifically designed to identify submerged seagrass. It is formulated as

$$\text{SSII} = \frac{\rho_{rc}(705)}{\rho_{rc}(865)+a} \tag{2}$$

where a is a small adjustment factor (e.g., 0.00001) used to prevent division by zero. Higher SSII values indicate greater seagrass density. The threshold values for both indices are generally determined empirically, based on expert knowledge and case-specific analysis.

The performance of SCM_SVM was evaluated mainly by three metrics: the producer's accuracy (PA), the overall identification accuracy (OIA), and the Kappa coefficient (K). PA is calculated by

$$\text{PA} = \frac{P_i}{A_i} \times 100\% \tag{3}$$

where A_i and P_i are the numbers of ground-truth and correctly identified pixels for each substrate type i, respectively.

The OIA is the percentage of correctly identified pixels relative to the total number of pixels, representing the overall

TABLE I
SUBSTRATE DETECTION ACCURACY (IN %) OF SCM_SVM IN THE TRAINING AND INDEPENDENT VALIDATION DATASETS WITH DIFFERENT INPUT VARIABLES

Model	Inputs	Training dataset		Ground-truth data	
		Sand	Seagrass	Sand	Seagrass
1	444, 533, and 612 nm	94.44%	86.42%	81.56%	74.71%
2	444, 492, 533, 566 and 612 nm	96.12%	89.74%	81.23%	77.95%
3	444, 492, 533, 566, 612 and 665 nm	96.86%	91.74%	83.80%	78.74%
4	444, 492, 533, 566, 612, 665, and 707 nm	97.40%	94.02%	82.37%	82.20%
5	444, 492, 533, 566, 612, 665, 707, and 866 nm	96.88%	95.45%	81.46%	85.18%
6	8 Band; Tide/Mean Tide	98.04%	97.80%	82.59%	85.00%
7	8 Band; cos(2pi*Lon/360); cos(2pi*Lat/180)	96.53%	94.70%	81.46%	85.24%
8	8 Band; cos(2pi*Lon/360); cos(2pi*Lat/180); Tide/Mean Tide	97.93%	97.66%	82.34%	84.66%

accuracy of substrate classification. It can be calculated by

$$\text{OIA} = \frac{\sum_{i=1}^{k}(P_i)}{N} \times 100\% \tag{4}$$

where N is the total number of pixels.

The Kappa coefficient, which ranges from 0 to 1, indicates the overall agreement between the distribution of classification results and ground-truth measurements, where larger K values indicate greater consistency [57]. K is calculated by

$$K = \frac{\text{OIA} - p_e}{1 - p_e} \tag{5}$$

where p_e represents the chance agreement, which is calculated based on the distributions of the actual and predicted substrate types and is expressed as

$$p_e = \frac{1}{N^2}\sum_{i=1}^{k}(A_i P_i) \tag{6}$$

where k is the number of categories ($k = 3$).

III. RESULTS AND DISCUSSION

A. Sensitivity of Inputs on the Performance of SCM_SVM

Model inputs are crucial factors that influence the performance of any algorithm. Table I presents the performance of SCM_SVM with different input configurations, including $\rho_{rc}(\lambda)$ at different spectral bands and additional environmental variables. The analysis using different spectral bands showed that the eight-band configuration most effectively captures seagrass features from SuperDove imagery. When compared to using $\rho_{rc}(\lambda)$ at only three bands, the eight-band input improved seagrass detection accuracy by 9%. Including an additional band led to an average 2% increase in seagrass substrate detection accuracy for both the training and independent validation datasets.

As shown in Table I, incorporating additional variables, such as geolocation and tide data, had a limited effect on model performance compared to using $\rho_{rc}(\lambda)$ at all eight spectral bands. Note that, in Table I, tide height was normalized, and latitude and longitude were cosine-transformed to maintain similar data characteristics with $\rho_{rc}(\lambda)$ and enhance the learning rate [58]. The optimal performance achieved using $\rho_{rc}(\lambda)$ at eight spectral bands and the neglected improvements from additional variables can be attributed to the following reasons.

$\rho_{rc}(\lambda)$ at the eight bands, ranging from the visible to NIR, can implicitly capture information related to the water body (such as concentrations of different constituents), topography (including substrates and depth), and atmospheric (aerosol) effects. Thus, it ensures a comprehensive representation of water and atmospheric properties, thereby improving model performance compared to models with fewer spectral bands as inputs.

Geolocation variables, such as latitude and longitude, have limited impact on the performance of SCM_SVM, as it was trained on data from a small lagoon. However, we anticipate that geolocations may become necessary inputs for models aimed at global seagrass detection. The negligible impact of tide data on model performance could be due to the fact that we used a single tide height value for the entire image, which might be impractical because tidal height could vary across LAL, particularly during ebb and flood tides. More importantly, the depth information, implicitly represented in the eight-band spectral $\rho_{rc}(\lambda)$, may partially account for tide variations. Given the negligible improvement in model performance and the potential increase in computational complexity when including these additional variables, we decided to use $\rho_{rc}(\lambda)$ at the eight bands as the model inputs.

B. Evaluation of SCM_SVM

The performance of SCM_SVM was first evaluated using the training dataset collected from LAL, with statistical results presented in Table II. The statistical metrics for the Train_set and Test_set were comparable, with negligible differences in the computed values. For the Test_set, the PA for seagrass, sand, and ODW was 94.1%, 94.2%, and 96.1%, respectively, with an OIA of 94.8%. The K value for the predicted

TABLE II

PERFORMANCE OF SCM_SVM IN THE TRAINING AND TESTING DATASETS (TRAIN_SET AND TEST_SET). P- AND T- STAND FOR PREDICTED AND TRUE SUBSTRATES, RESPECTIVELY. PA REPRESENTS THE PRODUCER'S ACCURACY, AND OIA INDICATES THE OVERALL IDENTIFICATION ACCURACY

	Train_set (N = 1.88×10^6)			**Test_set (N = 4.56×10^5)**		
	T-Seagrass	**T-Sand**	**T-ODW**	**T-Seagrass**	**T-Sand**	**T-ODW**
P-Seagrass	9.49	0.26	0.10	2.31	0.66	0.03
P-Sand	0.48	4.99	0.02	0.12	1.22	0.01
P-ODW	0.10	0.28	3.32	0.02	0.01	0.81
Total	10.69	5.29	3.45	2.46	1.29	0.84
PA	94.5%	94.2%	96.3%	94.1%	94.2%	96.1%
OIA		95.0%			94.8%	
K		0.91			0.91	

substrates in Test_set is 0.91, indicating a high level of agreement between the classification results and the ground-truth measurements. These results suggest that SCM_SVM has promising identification accuracy for these different substrates, at least within the LAL.

To further assess the applicability of SCM_SVM, we applied the model to two SuperDove images of LAL acquired during relatively high and low tides on November 5, 2022 and November 13, 2022, respectively. Evaluations of these two images provided independent validation of SCM_SVM, as they were not part of the training dataset construction. The predicted substrate distributions were validated against ground-truth data from the sonar. Note that each SuperDove pixel (∼9 m^2) may correspond to multiple ground-truth records from underway sonar data. Thus, the following criteria were applied for satellite and in situ matchups. If more than 50% of the ground-truth records within a matched pixel indicated seagrass presence, this pixel was classified as seagrass substrate. Otherwise, it was categorized into sand substrate. The derived substrate distributions from both SuperDove images are presented in Figs. 5 and 6. Here, all pixels identified as ODW by SCM_SVM are classified as sand substrates for model validation against ground-truth data.

As illustrated in Figs. 5 and 6, seagrass meadows are primarily concentrated in the southern region of LAL, with scattered patches along the eastern and western coasts. This distribution pattern is generally consistent with the reported seagrass distribution from field surveys for the same lagoon in 2019 and 2022 [24], [59]. Notably, the distribution pattern of seagrass coincides with the dark gray areas in the RGB imagery, demonstrating strong consistency between satellite retrievals and visual interpretation. Furthermore, the seagrass distribution pattern shows good agreement with the ground-truth observations from field surveys conducted within two weeks of image acquisition [e.g., Figs. 5(e) and 6(e)]. Statistically, the PA of SCM_SVM in identifying seagrass substrates reached 86.69% and 83.49% for images acquired on November 5, 2022 and November 13, 2022, respectively.

Note that both WAVI and SSII are able to identify seagrass for the low-tide image, but they significantly underestimate the seagrass extent, even in the southern LAL, where seagrass is dense. Specifically, ∼90% and ∼55% of seagrass substrate was misclassified as sand (False Seagrass, FSG) by WAVI and SSII, respectively. In contrast, only ∼16.5% FSG were observed for SCM_SVM. More importantly, the performance of the two index-based models significantly deteriorated for the high-tide image, with both models exhibiting misclassification rates of over 95% for seagrass, compared to an FSG rate of ∼13.3% by SCM_SVM. These comparison results indicate that the two index-based models are ineffective for high-tide scenarios, at least for the seagrass detection in LAL. While potential improvements could be achieved by tuning the empirical constants in (1) and (2) or adjusting the threshold for seagrass detection, these adjustments are arbitrary and, in fact, provide only a slight enhancement in seagrass detection accuracy. Nevertheless, SCM_SVM shows much more consistent performance in identifying seagrass across various tidal conditions (FSG rates ranging from 13.3% to 16.5%), underscoring its strong capability in generating consistent and accurate time-series seagrass mapping products in LAL.

The misclassification rates, ranging from ∼13% to ∼20% for seagrass and sand substrates, can be attributed to three main factors. First, uncertainties in the ground-truth data from field surveys played a role. A 0.1-m threshold for seagrass canopy height was used to identify seagrass substrates from the sonar measurements (Section II-B), which may misclassify seagrass canopies shorter than this height as sand substrates, such as juvenile seagrass or seagrass tilted by tides. Additionally, pixels with macroalgae may exhibit similar spectral signals to those of seagrass in remote sensing data; however, these pixels were also classified as sand in the ground-truth data. These factors contribute to the relatively high misclassification rates of the sand substrate by SCM_SVM for the two SuperDove images (Table III).

Second, each satellite observation (∼9 m^2) could correspond to multiple ground-truth records from sonar, potentially

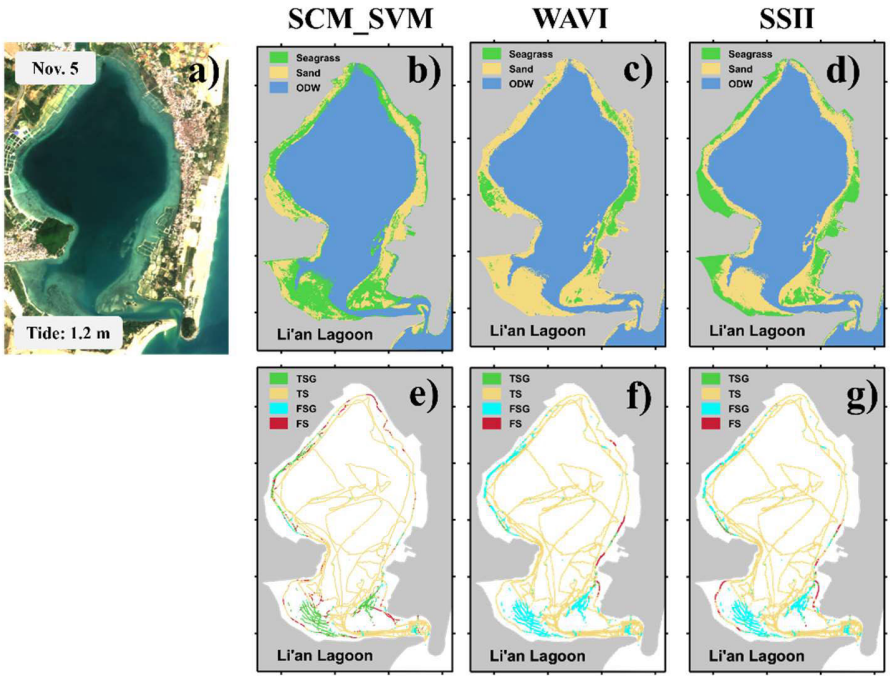

Fig. 5. Independent validation of seagrass detection algorithms using field survey measurements. (a) True-color composite image of SuperDove, acquired under relatively high tide on November 5, 2022. (b)–(d) Substrate distributions derived from SCM_SVM, WAVI, and SSII, respectively, where green, light yellow, and light blue patches represent seagrass, sand, and ODW, respectively. (e)–(g) Classification results of the three methods against ground-truth data. Green, light yellow, cyan, and red colors represent correctly identified seagrass (True Seagrass, TSG), correctly identified sand (True Sand, TS), seagrass misclassified as sand (False Seagrass, FSG), and sand misclassified as seagrass (False Sand, FS), respectively.

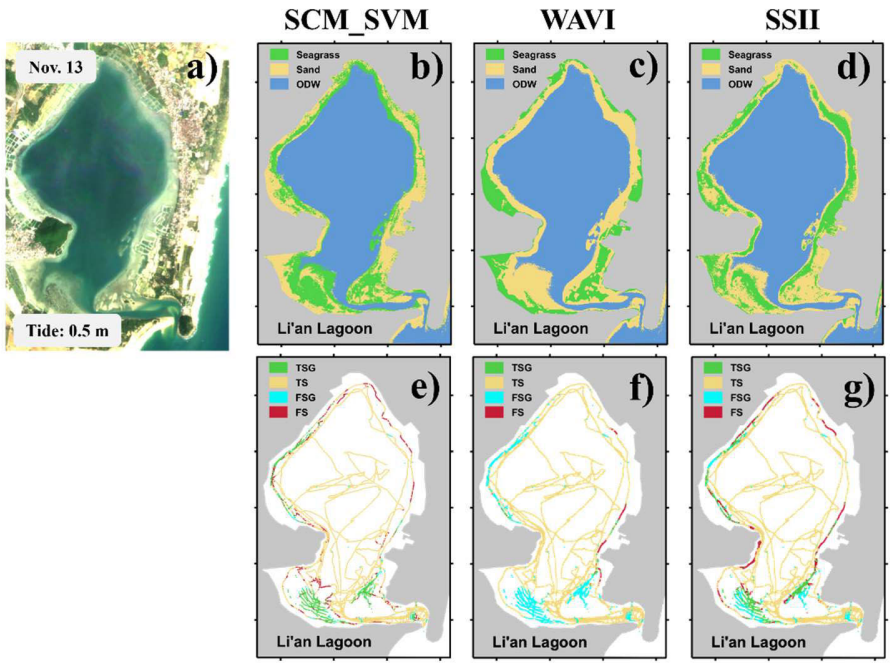

Fig. 6. Same as Fig. 5, but for the SuperDove image acquired under low tide on November 13, 2022.

causing discrepancies between satellite observations and ground-truth data, particularly in areas with mixed substrates. In general, the bottom reflectance of a sand substrate is significantly stronger than that of seagrass. Therefore, pixels with sparse seagrass may be misclassified as sand substrate from remote sensing, even though the ground-truth data categorize them as seagrass. As a result, misclassification primarily occurred in pixels with mixed substrates, such as those located at the edge of the seagrass meadows or the boundaries of ODW. Finally, the adjacency effects from land may distort $\rho_{rc}(\lambda)$ in nearshore pixels, which could partially explain the misclassification observed in some nearshore regions.

TABLE III

STATISTICS FOR THE CORRECTED AND INCORRECTLY RECOGNIZED PIXELS FOR SUBSTRATES DERIVED BY SCM_SVM, WAVI, AND SSII COMPARED TO THE GROUND-TRUTH DATA FOR THE TWO IMAGES ACQUIRED ON NOVEMBER 5 AND 13, 2022. P- AND T- STAND FOR PREDICTED AND TRUE SUBSTRATES, RESPECTIVELY

		Nov. 5th		Nov. 13th	
		T-Seagrass	T-Sand	T-Seagrass	T-Sand
SCM_SVM	P-Seagrass	2326	3236	2240	4130
	P-Sand	357	16685	443	15791
	PA	86.69%	83.76%	83.49%	79.27%
WAVI	P-Seagrass	64	637	280	551
	P-Sand	2619	19284	2403	19370
	PA	2.38%	97.80%	10.44%	97.23%
SSII	P-Seagrass	115	836	1212	3028
	P-Sand	2568	19085	1471	16893
	PA	4.29%	96.80%	45.17%	84.80%

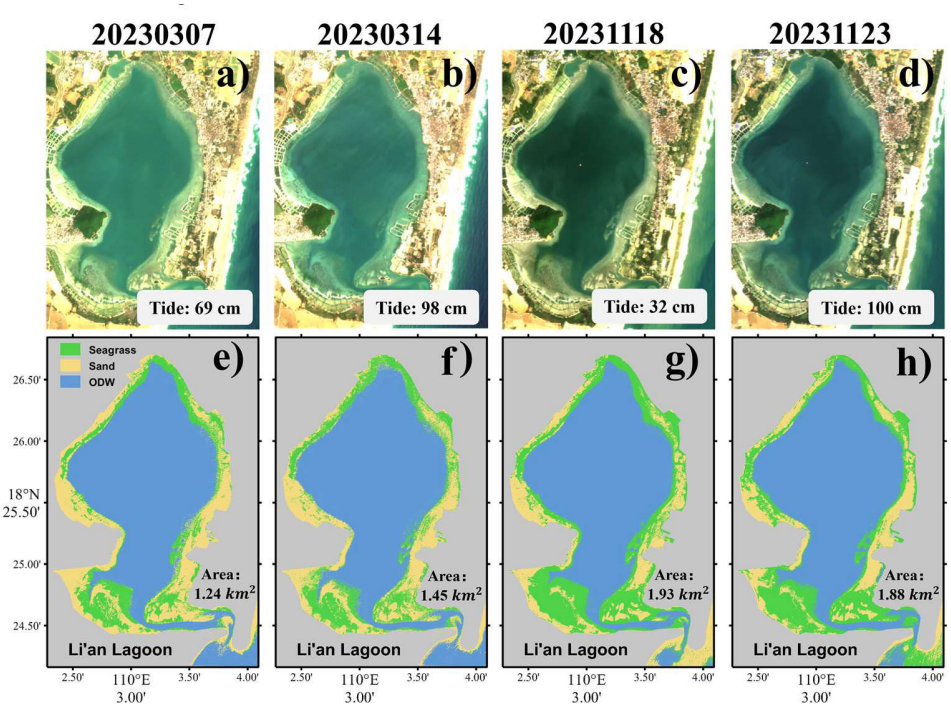

Fig. 7. Comparison of seagrass distribution in LAL from SuperDove images acquired under high and low tides. (a)–(d) Show the true-color composited image acquired on March 7, 2023, March 14, 2023, November 18, 2023, and November 23, 2023, with the tide levels labeled in the textbox. (e)–(h) Display the retrieved seagrass distribution by SCM_SVM for the corresponding image, along with the computed seagrass area.

C. Performance of SCM_SVM Under Various Tide Conditions

As the contribution of seagrass reflectance to the water-leaving radiometric signal would be significantly damped with increasing tide levels, tide levels have long been a significant limiting factor in the remote identification of seagrass in nearshore shallow waters [22]. Therefore, the robustness of a developed remote sensing model for seagrass detection and classification needs to be evaluated for its performance on images acquired under varying tidal conditions. In this study, we applied the SCM_SVM model to four SuperDove images captured under high and low tides in March and November 2023, respectively.

As illustrated in Fig. 7, SCM_SVM predicts consistent seagrass distribution for images acquired during low and high tides. For instance, the interpreted seagrass distribution on March 7 by SCM_SVM, corresponding to a relatively low tide with a tide level of 69 cm, closely matches the result of March

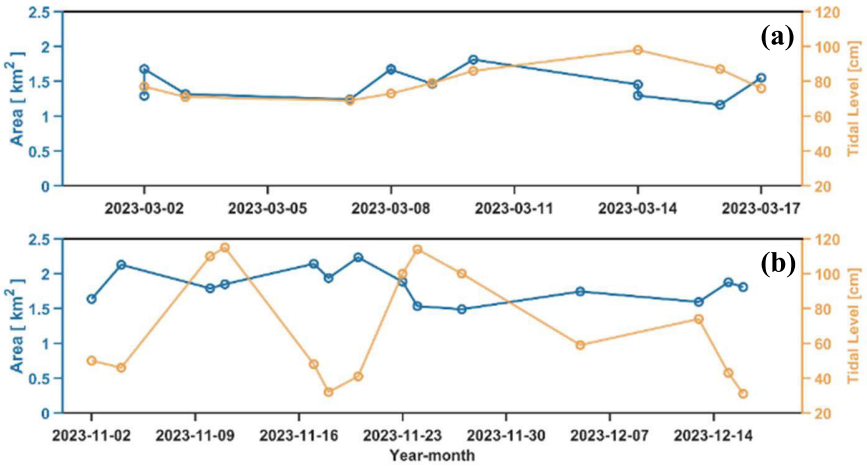

Fig. 8. Time series of the estimated seagrass area in LAL using SCM_SVM from SuperDove images acquired in (a) March and (b) November and December 2023. The tide levels at the time of each image acquisition are also included for comparison and aligned with the right y-axis.

14, which was acquired under a relatively high tide with a tide level of 98 cm [see Fig. 7(e) and (f)]. The estimated seagrass areas for the two images are also comparable (1.24 versus 1.45 km^2). Similarly, the November 2023 case demonstrates consistent seagrass mapping by SCM_SVM, in terms of both spatial patterns and estimated areas, for images acquired under different tide conditions [see Fig. 7(g) and (h)]. Despite a substantial tidal difference of 66 cm, the estimated seagrass area between the two images differs by only $\sim$0.05 km^2. These results suggest that SCM_SVM can retrieve consistent seagrass distribution for images acquired across different tidal conditions.

In addition, SCM_SVM was applied to a series of cloud-free SuperDove images in the LAL in March, November, and December 2023. The time-series variations of the estimated seagrass area and tidal changes are shown in Fig. 8. These two periods were selected to represent two distinct tidal types: a neap tide in March 2023 and a spring tide from November to December 2023. It is essential to note that each selected period encompasses at least one complete tidal cycle (see Fig. 8), enabling a reliable assessment of SCM_SVM's performance under varying tidal conditions. As shown in Fig. 8, the predicted seagrass areas within the two respective periods are overall consistent despite variations in tide levels, demonstrating the robust and stable performance of SCM_SVM under various tidal conditions. In general, larger seagrass area estimates are observed for images acquired under relatively low tides and vice versa. This is reasonable, as higher tide levels could reduce the contribution of seagrass reflectance to $\rho_{rc}(\lambda)$, potentially leading to failed seagrass detection from remote sensing and an underestimation of seagrass area.

Nevertheless, the variations in the calculated seagrass area were relatively small in the two examples shown in Fig. 8. For instance, the remotely estimated seagrass area was 1.5 ± 0.3 km^2 for the 11 SuperDove images acquired between March 2, and 17, with tide levels ranging from 69 to 98 cm [see Fig. 8(a)]. Notably, despite significant tidal variations from 20 to 120 cm between November 2, 2023 and December 17, 2023 [see Fig. 8(b)], the estimated seagrass area by SCM_SVM was averaged at 1.8 km^2 for the 14 SuperDove images, with a standard deviation of only 0.4 km^2. These relatively small standard deviations underscore the robustness of SCM_SVM in identifying seagrass across varying tidal conditions.

D. Trend in Seagrass Area From 2021 to 2023

The high revisit frequency of SuperDove enables sufficient observations, allowing for high spatial and temporal resolution monitoring of seagrass distribution. This capability facilitates the study of seagrass evolution and trend analysis in LAL, providing valuable insights for the assessment and conservation of seagrass ecosystems. In this study, we applied SCM_SVM to 157 cloud-free SuperDove images acquired between January 2021 and January 2024. The monthly variations in the estimated seagrass area are presented in Fig. 9. Note that there are relatively fewer images available during the summer months due to the rainy season.

As shown in Fig. 9, seagrass in LAL exhibits a seasonal pattern, with higher abundances in boreal spring and winter and relatively lower abundances in boreal summer. This seasonal pattern is likely modulated by the combined impacts of light intensity and water temperature [60], with similar patterns also reported in other seagrass meadows in tropical regions [59], [61]. The standard deviations of the estimated seagrass area in most months are relatively small, confirming the robust and stable performance of SCM_SVM across images acquired within each month. However, some months, such as September 2021, exhibit relatively large standard deviations in the estimated seagrass area. During these months, SCM_SVM failed to identify the seagrass substrate in some images, which could be attributed to thin haze and wind- or tide-driven sediment resuspension. On the one hand, a thin haze may not be easily ruled out by visual inspection of cloud-free images and could confuse the SCM_SVM system. On the other hand, for pixels with strong resuspension, the predicted substrate by SCM_SVM is either sand or ODW. These factors may contribute to the relatively large standard deviations in certain months.

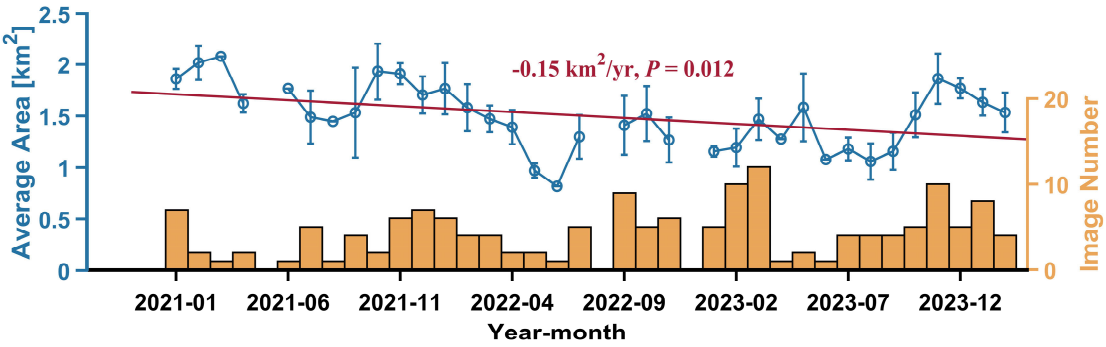

Fig. 9. Monthly variations in estimated seagrass area in LAL from January 2021 to January 2024. The blue circle represents the averaged seagrass area computed from all available SuperDove images acquired within each month, while the error bar indicates the standard deviation. The bar chart, aligned with the right y-axis, shows the total number of SuperDove images used in each month.

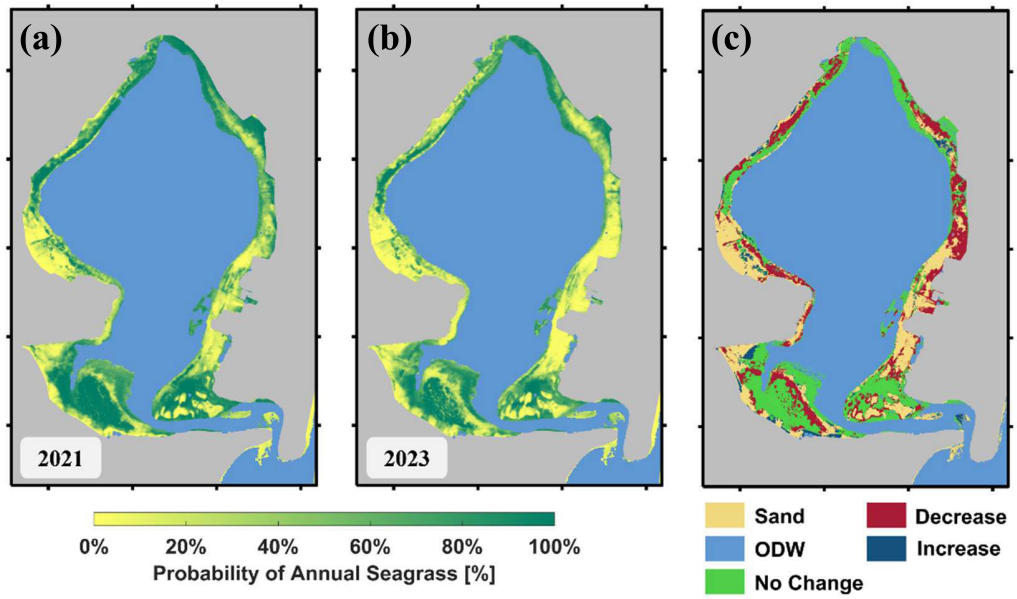

Fig. 10. Relative changes in seagrass distribution in LAL between 2021 and 2023. (a) and (b) Probability distribution of seagrass (P) in 2021 and 2023, respectively. (c) Relative changes in seagrass between 2021 and 2023, which is defined as the difference of P between 2023 and 2021. In (c), green represents no change in seagrass, red indicates a decrease, and dark blue signifies an increase.

Despite substantial seasonal variations, a declining trend in the seagrass area was observed during the investigated period at a rate of -0.15 km^2/yr (Fig. 9). This linear trend is statistically significant, with a p-value of 0.012 ($p < 0.05$). The seagrass meadows maintained a relatively high extent in 2022, with an annual mean area of 1.76 km^2, but decreased to an average of 1.33 km^2 in 2023, resulting in a 24% reduction. Since July 2022, the seagrass extent has remained relatively stable for almost a year until August 2023 when it then increased toward the end of the year.

To analyze the spatial–temporal variations in seagrass extent in LAL, we generated the probability distribution maps of seagrass for 2021 and 2023, respectively [see Fig. 10(a) and (b)]. The probability distribution of seagrass (P) for a specific pixel can be expressed as

$$P = \frac{N_{\text{Seagrass}}}{N_{\text{valid}}} \tag{7}$$

where N_{Seagrass} represents the number of images with detected seagrass at this pixel and N_{valid} represents the total number of images used in each year [62], [63].

Note that for each year, we have employed over 50 images from different seasons (see the histogram in Fig. 9) to ensure that the calculated P accurately reflects the actual frequency of seagrass presence at each pixel. The relative change in seagrass for each pixel is categorized into three classes: no change, decrease, and increase. This classification is based on the difference in P values between 2023 and 2021. Specifically, if the P difference falls within ± 0.25, the pixel is considered to have no significant change in seagrass. A P value difference greater than 0.25 indicates a confident increase, while a difference less than -0.25 suggests a confident decrease in seagrass.

As shown in Fig. 10(c), notable spatial changes in seagrass extent were observed, with only a few isolated nearshore locations showing slight increases, while widespread losses occurred across the lagoon between 2021 and 2023. Statistically, approximately 1.30 km^2 of seagrass remained stable, whereas 0.40 km^2 was lost. The most substantial reductions happened in the eastern and northwestern regions of LAL. Seagrass coverage has generally declined in the southern region, with widespread reductions along the outer edges of

previously seagrass-dense areas. The decline of seagrass could be primarily attributed to nearshore aquaculture activities and the construction of a theme park in the northwestern part of LAL since 2022 [59], [64]. Similar patterns have been reported in other coastal ecosystems, where urban expansion, coastal infrastructure development, and pollution can contribute to seagrass degradation [32], [65].

On the one hand, the construction activities directly removed or buried seagrass meadows in the northwest LAL and adjacent areas. On the other hand, dredging and land reclamation increased sediment resuspension, which smothered seagrass meadows and blocked sunlight essential for photosynthesis, ultimately inhibiting their growth [37], [66]. Nevertheless, these results highlight the importance of remote sensing techniques in monitoring seagrass evolution at high spatial–temporal resolution, as well as in understanding its responses to human activities.

IV. Conclusion

This study introduces a novel framework for accurate and consistent seagrass detection across varying tide conditions. The success of this framework stems from the innovative construction of a large training dataset, which pairs confident ground-truth substrate information from low-tide images with radiometric measurements from a range of images spanning low to high tides. This compilation is only possible due to the high revisit frequency of SuperDove, where most low-tide images can be easily matched with multiple low-to-high-tide images within a short period, ensuring a sufficient number of matchups to train the machine learning model. Validation with field sonar measurements indicates that the proposed substrate classification model (SCM_SVM) achieves a satisfactory accuracy of ∼85% in detecting seagrass substrates for both relatively high- and low-tide images. Applying SCM_SVM to time-series SuperDove images further confirmed its reliability for consistent mapping seagrass distribution in LAL under varying tidal conditions. Thus, SCM_SVM effectively addresses the longstanding limitation of traditional index-based algorithms, which could only map seagrass under low-tide conditions.

More importantly, the development of SCM_SVM, including the compilation of training data and machine learning-based substrate classification, provides a valuable reference framework for seagrass mapping in other regions. Future advancements in seagrass remote sensing may focus on two aspects: 1) expanding the training dataset to classify seagrass species and extending the application of SCM_SVM to diverse geographic regions and 2) integrating multisource high-resolution imagery, such as Sentinel-2 and the Landsat series, to ensure consistent and long-term monitoring of seagrass distribution. The latter is especially crucial for understanding seagrass responses to anthropogenic pressures and climate change while supporting conservation efforts, habitat protection, and blue carbon assessments.

Acknowledgment

SuperDove images were freely accessed through the education and research program on the Planet website.

References

[1] R. J. Orth, S. R. Marion, K. A. Moore, and D. J. Wilcox, "Eelgrass (*Zostera marina* L.) in the Chesapeake bay region of mid-Atlantic coast of the USA: Challenges in conservation and restoration," *Estuaries Coasts*, vol. 33, no. 1, pp. 139–150, Jan. 2010.

[2] F. T. Short et al., "Extinction risk assessment of the world's seagrass species," *Biol. Conservation*, vol. 144, no. 7, pp. 1961–1971, 2011.

[3] L. J. McKenzie, L. M. Nordlund, B. L. Jones, L. C. Cullen-Unsworth, C. Roelfsema, and R. K. F. Unsworth, "The global distribution of seagrass meadows," *Environ. Res. Lett.*, vol. 15, no. 7, Jul. 2020, Art. no. 074041, doi: 10.1088/1748-9326/ab7d06.

[4] C. M. Duarte, I. J. Losada, I. E. Hendriks, I. Mazarrasa, and N. Marbà, "The role of coastal plant communities for climate change mitigation and adaptation," *Nature Climate Change*, vol. 3, no. 11, pp. 961–968, Nov. 2013.

[5] M. Potouroglou et al., "Measuring the role of seagrasses in regulating sediment surface elevation," *Sci. Rep.*, vol. 7, no. 1, p. 11917, Sep. 2017.

[6] J. W. Fourqurean et al., "Seagrass ecosystems as a globally significant carbon stock," *Nature Geosci.*, vol. 5, no. 7, pp. 505–509, Jul. 2012.

[7] M. Stankovic et al., "Blue carbon assessments of seagrass and mangrove ecosystems in south and Southeast Asia: Current progress and knowledge gaps," *Sci. Total Environ.*, vol. 904, Dec. 2023, Art. no. 166618.

[8] Y. Ren et al., "Seagrass decline weakens sediment organic carbon stability," *Sci. Total Environ.*, vol. 937, Aug. 2024, Art. no. 173523.

[9] C. M. Duarte, J. J. Middelburg, and N. Caraco, "Major role of marine vegetation on the oceanic carbon cycle," *Biogeosciences*, vol. 2, no. 1, pp. 1–8, Feb. 2005.

[10] C. M. Duarte et al., "Seagrass community metabolism: Assessing the carbon sink capacity of seagrass meadows," *Global Biogeochem. Cycles*, vol. 24, no. 4, Dec. 2010, Art. no. GB4032, doi: 10.1029/2010GB003793.

[11] P. I. Macreadie, M. E. Baird, S. M. Trevathan-Tackett, A. W. D. Larkum, and P. J. Ralph, "Quantifying and modelling the carbon sequestration capacity of seagrass meadows—A critical assessment," *Mar. Pollut. Bull.*, vol. 83, no. 2, pp. 430–439, Jun. 2014.

[12] A. B. Hansen, A. S. Pedersen, M. Kühl, and K. E. Brodersen, "Temperature effects on leaf and epiphyte photosynthesis, bicarbonate use and diel O_2 budgets of the seagrass *Zostera marina* L.," *Frontiers Mar. Sci.*, vol. 9, Mar. 2022, Art. no. 822485.

[13] J. B. Lamb et al., "Seagrass ecosystems reduce exposure to bacterial pathogens of humans, fishes, and invertebrates," *Science*, vol. 355, no. 6326, pp. 731–733, Feb. 2017.

[14] M. Waycott et al., "Accelerating loss of seagrasses across the globe threatens coastal ecosystems," *Proc. Nat. Acad. Sci. USA*, vol. 106, no. 30, pp. 12377–12381, Jul. 2009.

[15] F. T. Short et al., "Monitoring in the western Pacific region shows evidence of seagrass decline in line with global trends," *Mar. Pollut. Bull.*, vol. 83, no. 2, pp. 408–416, Jun. 2014.

[16] X. Shen et al., "Spatial variability in blue carbon storage and sequestration of seagrass meadows in southern China," *Sci. Total Environ.*, vol. 951, Nov. 2024, Art. no. 175884.

[17] W. F. De Boer, "Seagrass–sediment interactions, positive feedbacks and critical thresholds for occurrence: A review," *Hydrobiologia*, vol. 591, no. 1, pp. 5–24, Oct. 2007.

[18] M. S. Hossain, J. S. Bujang, M. H. Zakaria, and M. Hashim, "The application of remote sensing to seagrass ecosystems: An overview and future research prospects," *Int. J. Remote Sens.*, vol. 36, no. 1, pp. 61–114, Jan. 2015.

[19] S. Xu et al., "Single beam sonar reveals the distribution of the eelgrass *Zostera marina* L. and threats from the green tide algae *Chaetomorpha linum* K. In swan-lake lagoon (China)," *Mar. Pollut. Bull.*, vol. 145, pp. 611–623, Aug. 2019.

[20] B. K. Veettil, R. D. Ward, M. D. A. C. Lima, M. Stankovic, P. N. Hoai, and N. X. Quang, "Opportunities for seagrass research derived from remote sensing: A review of current methods," *Ecological Indicators*, vol. 117, Oct. 2020, Art. no. 106560.

[21] R. Garcia, J. Hedley, H. Tin, and P. Fearns, "A method to analyze the potential of optical remote sensing for benthic habitat mapping," *Remote Sens.*, vol. 7, no. 10, pp. 13157–13189, Oct. 2015.

[22] M. L. Zoffoli et al., "Sentinel-2 remote sensing of *zostera noltei*-dominated intertidal seagrass meadows," *Remote Sens. Environ.*, vol. 251, Dec. 2020, Art. no. 112020.

[23] T. Kutser, J. Hedley, C. Giardino, C. Roelfsema, and V. E. Brando, "Remote sensing of shallow waters—A 50 year retrospective and future directions," *Remote Sens. Environ.*, vol. 240, Apr. 2020, Art. no. 111619.

[24] Y. Li, J. Bai, L. Zhang, and Z. Yang, "Mapping and spatial variation of seagrasses in Xincun, Hainan province, China, based on satellite images," *Remote Sens.*, vol. 14, no. 10, p. 2373, May 2022.

[25] H. M. Dierssen, K. J. Bostrom, A. Chlus, K. Hammerstrom, D. R. Thompson, and Z. Lee, "Pushing the limits of seagrass remote sensing in the turbid waters of Elkhorn slough, California," *Remote Sens.*, vol. 11, no. 14, p. 1664, Jul. 2019.

[26] D. Traganos and P. Reinartz, "Mapping Mediterranean seagrasses with Sentinel-2 imagery," *Mar. Pollut. Bull.*, vol. 134, pp. 197–209, Sep. 2018.

[27] R. A. Garcia, Z. Lee, B. B. Barnes, C. Hu, H. M. Dierssen, and E. J. Hochberg, "Benthic classification and IOP retrievals in shallow water environments using MERIS imagery," *Remote Sens. Environ.*, vol. 249, Nov. 2020, Art. no. 112015, doi: 10.1016/j.rse.2020.112015.

[28] Z. Lee, K. L. Carder, C. D. Mobley, R. G. Steward, and J. S. Patch, "Hyperspectral remote sensing for shallow waters: 2. Deriving bottom depths and water properties by optimization," *Appl. Opt.*, vol. 38, no. 18, pp. 3831–3843, Jun. 1999.

[29] W. Sun et al., "Mapping China's coastal aquaculture ponds expansion with Sentinel-2 images during 2017–2021," *Int. J. Digit. Earth*, vol. 17, no. 1, Dec. 2024, Art. no. 2297943, doi: 10.1080/17538947.2023.2297943.

[30] P. Wicaksono, M. Hafizt, S. D. Harahap, and M. R. Nandika, "Integrating Sentinel-2 and PlanetScope image with drone-based seagrass data for seagrass percent cover mapping," *IOP Conf. Ser., Earth Environ. Sci.*, vol. 1291, no. 1, Jan. 2024, Art. no. 012012.

[31] D. Effrosynidis, A. Arampatzis, and G. Sylaios, "Seagrass detection in the mediterranean: A supervised learning approach," *Ecological Informat.*, vol. 48, pp. 158–170, Nov. 2018.

[32] K. J. E. Clemente, M. S. Thomsen, and R. C. Zimmerman, "The vulnerability and resilience of seagrass ecosystems to marine heatwaves in New Zealand: A remote sensing analysis of seascape metrics using PlanetScope imagery," *Remote Sens. Ecology Conservation*, vol. 9, no. 6, pp. 803–819, Dec. 2023, doi: 10.1002/rse2.343.

[33] P. Wicaksono and W. Lazuardi, "Assessment of PlanetScope images for benthic habitat and seagrass species mapping in a complex optically shallow water environment," in *Fine Resolution Remote Sensing of Species in Terrestrial and Coastal Ecosystems*. Evanston, IL, USA: Routledge, 2021, pp. 143–169.

[34] L. Wang et al., "Estimating four-decadal variations of seagrass distribution using satellite data and deep learning methods in a marine lagoon," *Sci. Total Environ.*, vol. 919, Apr. 2024, Art. no. 170936.

[35] M. M. Coffer et al., "Providing a framework for seagrass mapping in United States coastal ecosystems using high spatial resolution satellite imagery," *J. Environ. Manage.*, vol. 337, Jul. 2023, Art. no. 117669.

[36] M. Chowdhury et al., "AI-driven remote sensing enhances Mediterranean seagrass monitoring and conservation to combat climate change and anthropogenic impacts," *Sci. Rep.*, vol. 14, no. 1, p. 8360, Apr. 2024, doi: 10.1038/s41598-024-59091-7.

[37] A. Bargain, M. Robin, E. Le Men, A. Huete, and L. Barillé, "Spectral response of the seagrass *Zostera noltii* with different sediment backgrounds," *Aquatic Botany*, vol. 98, no. 1, pp. 45–56, Apr. 2012.

[38] H. Liang et al., "Remote sensing detection of seagrass distribution in a marine lagoon (Swan Lake), China," *Opt. Exp.*, vol. 31, no. 17, pp. 27677–27695, 2023.

[39] P. Villa, A. Laini, M. Bresciani, and R. Bolpagni, "A remote sensing approach to monitor the conservation status of lacustrine phragmites Australis beds," *Wetlands Ecology Manage.*, vol. 21, no. 6, pp. 399–416, Dec. 2013, doi: 10.1007/s11273-013-9311-9.

[40] S. R. Phinn, E. M. Kovacs, C. M. Roelfsema, R. F. Canto, C. J. Collier, and L. J. McKenzie, "Assessing the potential for satellite image monitoring of seagrass thermal dynamics: For inter- and shallow sub-tidal seagrasses in the inshore great barrier reef world heritage area, Australia," *Int. J. Digit. Earth*, vol. 11, no. 8, pp. 803–824, Aug. 2018.

[41] E. Kovacs, C. Roelfsema, M. Lyons, S. Zhao, and S. Phinn, "Seagrass habitat mapping: How do Landsat 8 OLI, Sentinel-2, ZY-3A, and Worldview-3 perform?" *Remote Sens. Lett.*, vol. 9, no. 7, pp. 686–695, Jul. 2018.

[42] E. L. Hestir, D. H. Schoellhamer, J. Greenberg, T. Morgan-King, and S. L. Ustin, "The effect of submerged aquatic vegetation expansion on a declining turbidity trend in the Sacramento-San Joaquin river delta," *Estuaries Coasts*, vol. 39, no. 4, pp. 1100–1112, Jul. 2016.

[43] E. L. Westlake, J. K. Keesing, L. K. Hardiman, M. Tonks, and Y. Olsen, "Growth, biomass and productivity of the seagrass *Thalassia hemprichii* at Ashmore Reef, Australia," *Aquatic Botany*, vol. 183, Dec. 2022, Art. no. 103557, doi: 10.1016/j.aquabot.2022.103557.

[44] M. Munir and P. Wicaksono, "Support vector machine for seagrass percent cover mapping using PlanetScope image in Labuan bajo, east Nusa Tenggara," *Proc. SPIE*, vol. 11372, pp. 582–587, Aug. 2019.

[45] N.-T. Ha, H.-Q. Nguyen, T.-D. Pham, C.-T. Hoang, and I. Hawes, "Superpixel for seagrass mapping: A novel method using PlanetScope imagery and machine learning in Tauranga harbour, New Zealand," *Environ. Earth Sci.*, vol. 82, no. 6, p. 154, Mar. 2023.

[46] A. Collison, A. Jumpasut, and H. Bourne, "On-orbit radiometric calibration of the planet satellite fleet," Planet Labs PBC, Jan. 2022. [Online]. Available: https://assets.planet.com/docs/radiometric_calibration_white_paper.pdf

[47] Q. Vanhellemont, "Evaluation of eight band SuperDove imagery for aquatic applications," *Opt. Exp.*, vol. 31, no. 9, pp. 13851–13874, 2023.

[48] N. Pahlevan et al., "ACIX-Aqua: A global assessment of atmospheric correction methods for Landsat-8 and Sentinel-2 over lakes, rivers, and coastal waters," *Remote Sens. Environ.*, vol. 258, Jun. 2021, Art. no. 112366.

[49] L. Feng, X. Hou, J. Li, and Y. Zheng, "Exploring the potential of Rayleigh-corrected reflectance in coastal and inland water applications: A simple aerosol correction method and its merits," *ISPRS J. Photogramm. Remote Sens.*, vol. 146, pp. 52–64, Dec. 2018.

[50] W. Lai, Z. Lee, J. Wang, Y. Wang, R. Garcia, and H. Zhang, "A portable algorithm to retrieve bottom depth of optically shallow waters from top-of-atmosphere measurements," *J. Remote Sens.*, vol. 2022, Jan. 2022, doi: 10.34133/2022/9831947.

[51] S. Ghosh, A. Dasgupta, and A. Swetapadma, "A study on support vector machine based linear and non-linear pattern classification," in *Proc. Int. Conf. Intell. Sustain. Syst. (ICISS)*, Feb. 2019, pp. 24–28.

[52] S. Hafeez et al., "Comparison of machine learning algorithms for retrieval of water quality indicators in case-II waters: A case study of Hong Kong," *Remote Sens.*, vol. 11, no. 6, p. 617, Mar. 2019, doi: 10.3390/rs11060617.

[53] G. Mountrakis, J. Im, and C. Ogole, "Support vector machines in remote sensing: A review," *ISPRS J. Photogramm. Remote Sens.*, vol. 66, no. 3, pp. 247–259, May 2011.

[54] D. C. Duro, S. E. Franklin, and M. G. Dubé, "A comparison of pixel-based and object-based image analysis with selected machine learning algorithms for the classification of agricultural landscapes using SPOT-5 HRG imagery," *Remote Sens. Environ.*, vol. 118, pp. 259–272, Mar. 2012.

[55] P. Villa, A. Mousivand, and M. Bresciani, "Aquatic vegetation indices assessment through radiative transfer modeling and linear mixture simulation," *Int. J. Appl. Earth Observ. Geoinf.*, vol. 30, pp. 113–127, Aug. 2014, doi: 10.1016/j.jag.2014.01.017.

[56] Y. Li, J. Bai, S. Chen, B. Chen, and L. Zhang, "Mapping seagrasses on the basis of Sentinel-2 images under tidal change," *Mar. Environ. Res.*, vol. 185, Mar. 2023, Art. no. 105880.

[57] J. Sim and C. C. Wright, "The Kappa statistic in reliability studies: Use, interpretation, and sample size requirements," *Phys. Therapy*, vol. 85, no. 3, pp. 257–268, Mar. 2005.

[58] N. Yang, H. Shi, H. Tang, and X. Yang, "Geographical and temporal encoding for improving the estimation of $PM_{2.5}$ concentrations in China using end-to-end gradient boosting," *Remote Sens. Environ.*, vol. 269, Feb. 2022, Art. no. 112828.

[59] S. Chen et al., "Analysis of seagrass bed distribution characteristics, health status, and influencing factors in Li'an harbor, Hainan," *Mar. Sci.*, vol. 44, no. 11, pp. 57–64, 2020.

[60] H. K. Plaisted et al., "Influence of rising water temperature on the temperate seagrass species eelgrass (*Zostera marina* L.) in the northeast USA," *Frontiers Mar. Sci.*, vol. 9, Jul. 2022, Art. no. 920699.

[61] M. Rasheed and R. Unsworth, "Long-term climate-associated dynamics of a tropical seagrass meadow: Implications for the future," *Mar. Ecology Prog. Ser.*, vol. 422, pp. 93–103, Jan. 2011.

[62] M. C. Hansen et al., "Humid tropical forest disturbance alerts using Landsat data," *Environ. Res. Lett.*, vol. 11, no. 3, Mar. 2016, Art. no. 034008, doi: 10.1088/1748-9326/11/3/034008.

[63] J.-F. Pekel, A. Cottam, N. Gorelick, and A. S. Belward, "High-resolution mapping of global surface water and its long-term changes," *Nature*, vol. 540, pp. 418–422, Dec. 2016, doi: 10.1038/nature20584.

[64] S. Yu et al., "Frequent flowering but low reproductive success of the dioecious seagrass *Enhalus acoroides* (L.F.) Royle in Li'an lagoon, China," *Estuaries Coasts*, vol. 47, no. 6, pp. 1694–1701, Sep. 2024, doi: 10.1007/s12237-024-01399-8.

[65] R. K. F. Unsworth et al., "Global challenges for seagrass conservation," *Ambio*, vol. 48, no. 8, pp. 801–815, Aug. 2019, doi: 10.1007/s13280-018-1115-y.

[66] I. Semesi, S. Beer, and M. Björk, "Seagrass photosynthesis controls rates of calcification and photosynthesis of calcareous macroalgae in a tropical seagrass meadow," *Mar. Ecology Prog. Ser.*, vol. 382, pp. 41–47, Apr. 2009.

Siyuan Hou was born in Shandong, China, in 1998. He is currently pursuing the Ph.D. degree in marine physics with Xiamen University, Xiamen, China.

His research interests include developing ocean color remote sensing algorithms for the identification of coral reefs and seagrass beds.

Xiaolong Yu received the B.S. degree in geoinformation science and technology from Tongji University, Shanghai, China, in 2010, the M.S. degree in cartography and geographic information system from East China Normal University, Shanghai, in 2013, and the Ph.D. degree in philosophy from the University of Twente, Enschede, The Netherlands, in 2019.

He was a Visiting Scholar with the University of Massachusetts Boston, Boston, MA, USA, from 2017 to 2019. He is currently with the State Key Laboratory of Marine Environmental Science, Xiamen University, Xiamen, China, as an Associate Professor. His research interests include radiative transfer theory and applications of ocean color remote sensing in optically complex waters.

Wendian Lai is currently pursuing the Ph.D. degree with the Department of Physical Oceanography, College of Ocean and Earth Sciences, Xiamen University, Xiamen, China.

His research interests include ocean color remote sensing algorithms for high-resolution bathymetry in shallow waters.

Fei Zhang received the master's degree from the Department of Marine Chemistry, Xiamen University, Xiamen, China, in 2022, where he is currently pursuing the Ph.D. degree with the Department of Applied Marine Physics and Engineering.

His research interests include marine ecological acoustics.

Hanyang Qiao received the B.S. degree from Yunnan University, Kunming, China, in 2017, and the M.S. degree from Lanzhou University, Lanzhou, China, in 2020. He is currently pursuing the Ph.D. degree with Xiamen University, Xiamen, China.

His research interests include ocean color remote sensing.

Peng Cheng received the B.S. and M.S. degrees in geography from Nanjing University, Nanjing, China, in 1995 and 1997, respectively, and the Ph.D. degree in marine and atmospheric science from the State University of New York at Stony Brook, Stony Brook, NY, USA, in 2007.

He presently works as a Professor with Xiamen University, Xiamen, China. His research interests include estuarine and coastal dynamics.

Zhongping Lee (Member, IEEE) was born in China, in 1964. He received the Ph.D. degree in physical oceanography from the University of South Florida, Tampa, FL, USA, in 1994, specializing in ocean color remote sensing.

He is now a Tang Shifeng Chair Professor with Xiamen University, Xiamen, China, and a fellow of the Optical Society of America. His research interests include radiative transfer in the aquatic environment, algorithms of ocean color remote sensing, and applications of satellite ocean color products. He has authored or co-authored more than 190 journal articles in this field.